PERGAMON

International Journal of Solids and Structures 40 (2003) 1653–1668

INTERNATIONAL JOURNAL OF SOLIDS and STRUCTURES

www.elsevier.com/locate/ijsolstr

Failure in the junction region of T-stiffeners: 3D-braided vs. 2D tape laminate stiffeners

Q.D. Yang *, K.L. Rugg, B.N. Cox, M.C. Shaw

Rockwell Scientific, 1049 Camino Dos Rios, Thousand Oaks, CA 91360, USA

Received 30 April 2002; received in revised form 5 December 2002

Abstract

Strain distributions and failure mechanisms are compared for a three-dimensionally (3D) braided T-stiffener (preform designed and supplied by 3TEX Inc.) and a conventional two-dimensional (2D) tape laminate T-stiffener, bonded onto a tape laminate skin. The strain distributions in a pull-off test are measured by laser speckle interferometry and calculated by computational simulations. With good agreement between experiment and theory, substantial differences are found between the two classes of stiffener. The tape laminate stiffeners exhibit large strain concentrations across the noodle region and in the adjacent radii, which correlate well with observed first cracking events. The 3D-braided stiffeners show relatively uniform strain distributions throughout the flanges, the web, and the flange/web junction region. Strain concentrations are modest at the corner of the junction and absent along the interface between the flanges and the skin. Failure in the 3D-braided stiffeners does not occur within the junction region, but by a sequence of cracking events, first next to the junction region and then at the end of one flange. The pull-off load at the first failure event is substantially higher for the 3D-braided stiffener than the tape laminate stiffener, which is attributed mainly to the relative absence of strain concentrations in the former.

In predicting strain distributions, account is taken of the details of the 3D architecture of the 3D-braided stiffeners as specified by the supplier (3TEX Inc.) by using the Binary Model of textile composites, whose formulation has been described previously. Comparison of the predicted and measured spatial distributions of strain constitutes a critical test of the Binary Model. It is found to perform well in this case.

Keywords: Textile composites; Failure analysis; Braided structure

1. Introduction

1.1. Alternative designs for stiffeners

T-stiffeners fabricated by laying up plies of unidirectional tape or 2D woven fabric (Fig. 1a) are often used to increase the stiffness of thin skin structures. While laminates have excellent in-plane mechanical

* Corresponding author. Tel.: +1-805-373-4316; fax: +1-805-373-4017.
E-mail address: qyang@rwsc.com (Q.D. Yang).

0020-7683/03/$ - see front matter © 2003 Elsevier Science Ltd. All rights reserved.
doi:10.1016/S0020-7683(03)00026-X

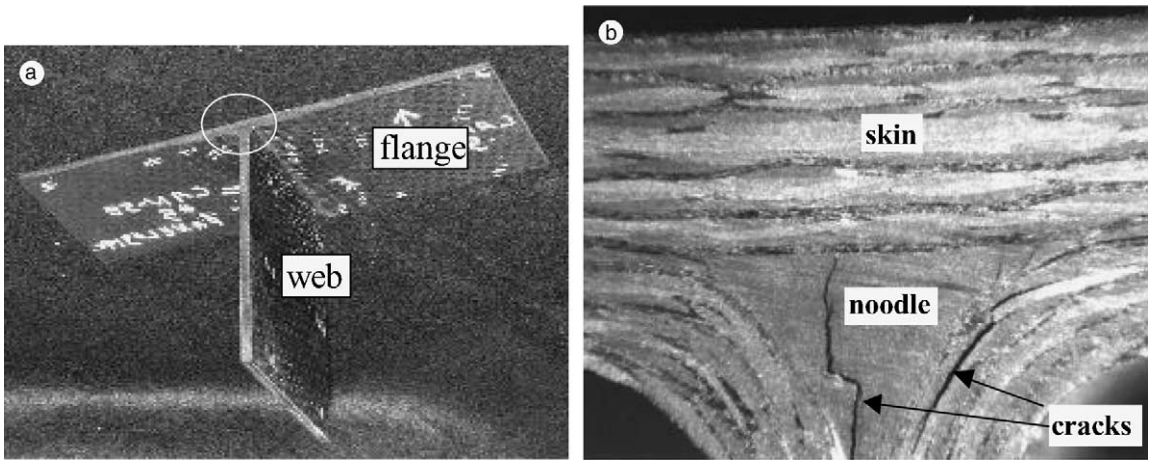

Fig. 1. (a) A typical 2D tape laminate T-stiffener. (b) Cracks formed in the noodle and radius segments under tensile loading along the web.

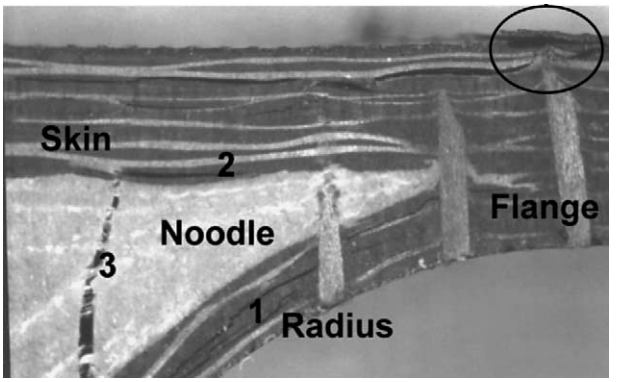

Fig. 2. Optical micrograph of a 4% z-fiber T-specimen showing the sequence of steps to failure: (1) delamination of the radius, (2) delamination of the skin, (3) cracking of noodle.

properties, they are prone to delamination due to impact or out-of-plane loads. Consequently, one mode of premature failure in tape laminate T-stiffeners is cracking in the radius of the web/flange junction. Premature failure can also be initiated by cracking of the noodle itself, which is a relatively brittle resin pocket. Even if the noodle is filled with fibers, it is still vulnerable to cracking parallel to the fiber direction. Thus the noodle region, which is a necessary feature of T-stiffeners formed by tape lay-up, is a poor design for strength. Fig. 1(b) shows typical cracks in a laminate T-stiffener loaded by tension along the web.

Through-thickness reinforcement such as fibrous or metallic rods (e.g., Z-fibers™ [1]) can bridge delamination cracks and greatly increase delamination resistance (Freitas et al., 1994; Freitas et al., 1996; Rugg et al., 2002). However, through-thickness reinforcement applied to T-stiffeners only increases the laminate strength in the webs and flanges. Pins inserted in the radius of the junction region appear to give little advantage and can even promote delamination initiation (Rugg et al., 2002). Fig. 2 shows the failure events

[1] Aztex Inc., Waltham, Massachusetts.

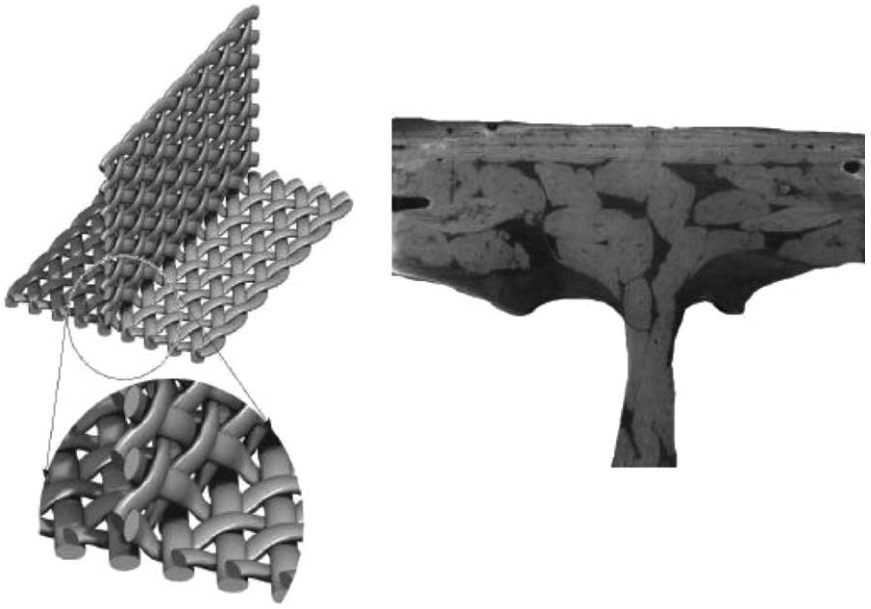

Fig. 3. (a) Computer generated schematic of the ideal tow arrangement in a 3D-braided T-stiffener preform (courtesy D. Mungalov, 3TEX Inc.). (b) The junction region of a consolidated sample (including skin).

in a 2D tape laminate stiffener reinforced by metallic rods. While these rods were effective in preventing in-plane crack propagation, they could not stop the noodle from cracking. Furthermore, fibers around the rods were significantly distorted during the insertion process, which would facilitate compressive micro-buckling.

Three-dimensional (3D) braiding offers an alternative method of fabricating T-stiffeners, with wide freedom available in the angles at which fiber rovings can be deployed and the proportions of fibers introduced at different angles (Bogdanovich and Mungalov, 2002). The 3D character of the process enables the T shape to be fabricated as an integral structure, with fibers passing continuously from the web to the flanges and back. The flexibility and 3D nature of 3D braiding and especially the particular machine described by Bogdanovich and Mungalov (2002) thus suggest that mechanically optimal stiffeners can be fabricated that will be robust against failure in the junction region. These benefits complement potential reductions in cost accruing from the elimination of labor-intensive lay-up steps.

Fig. 3a shows the architecture of one 3D-braided T-stiffener preform, which was designed and fabricated by 3TEX Inc. [2] and will be studied in this report. The fiber tows are braided in such a way that the noodle region is eliminated. While this is a potentially advantageous feature, the architecture of Fig. 3a has by no means been optimized for the function expected of a T-stiffener. It was used in first generation samples intended only to demonstrate the possibility of fabricating a T-stiffener using a prototype 3D braiding machine with a capacity for 64 braid yarns and 16 axial yarn ends (Bogdanovich and Mungalov, 2002). Nevertheless, these prototype specimens still exhibit some very interesting characteristics of load distribution and strength.

[2] 3TEX Inc., Cary, North Carolina.

1.2. Modeling 3D textiles

Braided and other 3D textile preforms present some particular challenges in analysis and design. Stiffness, failure mechanisms, and strength must depend on the local distribution of stresses and strains, which may fluctuate strongly over spatial gauges comparable to the tow diameter. Accurate predictions cannot be derived from models in which the material is homogenized. On the other hand, critical structural elements (such as the web/flange junction region) contain many segments of tows in different orientations, so that models based on meshes that are fine compared to the tow diameter are likely to contain prohibitively many degrees of freedom. A computational model that responds to this challenge, the Binary Model of textile composites, was formulated some years ago (Cox et al., 1994). The Binary Model may be viewed as a finite element formulation in which the textile composite is defined by two separate meshes. One mesh represents the axial stiffness of individual fiber tows by one-dimensional spring elements, which are located in space in one-to-one correspondence with the tow axes in the actual composite and are therefore faithful to the topology of the architecture. The other mesh defines solid elements that represent the matrix-dominated material properties (transverse stiffness, Poisson's effect, shear stiffness). The solid elements fill the space occupied by the component and therefore define its external geometry. This choice of formulation is very convenient for generating models of parts with complex shape reinforced by complex 3D architectures and is the most computationally efficient, physically admissible approach to predicting local stress and strain variations. Any coarser element choice could not follow variations on the scale of single tows; and a finer element choice may give rise to unnecessarily many degrees of freedom.

Other theoretical approaches to predicting the properties of 3D-braided or other textile composites fall into three chief categories. The first are isostrain or isostress models, in which either the strain or stress field is assumed to be uniform throughout the composite. These approximations lead to very simple results and are bounds to the true response under uniform applied fields. However, they cannot predict local stresses and strains, except in special cases, and they cannot deal with complex part shape or nonuniform applied fields. The second common approach is to use fine computational meshes (or other higher order numerical procedures) to model the behaviour of a unit cell of a periodic textile. This method provides details of local stress and strain fields, but it cannot be correct if the applied field varies significantly over distances comparable to the unit cell size; and it is applicable only to composites that are in fact periodic. Many textile structures are aperiodic; or periodic over such large scales that no significant simplification is achieved by considering a unit cell. The third class of models involves dividing the space occupied by a possibly complex textile structure into a tessellation of cells in correspondence with major heterogeneities. Within each cell, the material is regarded as homogeneous, with properties derived from those of the tows contained in the cell by a micromechanical model. The cells are coupled by approximate boundary conditions of continuity of displacements and/or tractions. In one early example of this approach, a 3D-braided T-stiffener was analyzed (Bogdanovich, 1993). However, because of the homogenization scheme used in that prior work, details of local stress or strain variations on the scale of individual tows were not calculated. Thus the Binary Model appears at present to be unique in its ability to account for both the details of fiber architecture down to the level of individual tows and the overall structural composite properties. Apart from the work of Bogdanovich (1993), no theoretical analysis of 3D-braided T-stiffeners based on other modeling methods has appeared in the literature.

One question of principal interest is the degree of accuracy that can be achieved in predicting local stresses and strains by the approximations of the Binary Model. From the point of view of utility in engineering applications, the best way of assessing this is to compare predictions of the model with measurements of local strain fields. The consistency with which strain fields can be measured is determined in large part by irregularity in the textile reinforcement. Since such irregularity is inevitable in textiles (at least in all fabrics made by current methods), a practical threshold for accuracy is that predictions should match measurements to within experimental variance. More refined theoretical knowledge of the behaviour of an

idealized (regular) textile structure is probably of no help in predicting the properties of the real, irregular composite.

One validation of the Binary Model has been carried out recently for a 3D woven angle-interlock composite of carbon fibers in a SiC matrix (Yang et al., 2002). This composite exhibits unusually strong local variations in strain components due to the textile architecture, partly because the specimens studied were quite thin (<1 mm thick). The Binary Model reproduced experimentally measured strain variations, which could not have been revealed by traditional continuum mechanics models, with encouraging fidelity. It also predicted the macroscopic stiffness, which was strongly affected by tow waviness.

In this report, the Binary Model will be applied to analyzing the prototype, 3D-braided T-stiffener of Fig. 3, in an exploration of the mechanics of failure of T-stiffeners. Model simulations and full-field strain measurements obtained by laser speckle interferometry will be used to assess the advantages of 3D-braided textile reinforcement for avoiding premature failure in the junction region of the T. Comparisons will be made with a typical 2D tape laminate T-stiffener.

2. Failure mechanisms

The 3D-braided stiffeners were fabricated at RSC using preforms supplied by 3TEX Inc. The stiffener preforms and skin fabric were infiltrated and cured together (Fig. 3b). The skins comprised a single warp-knitted stack of plies in a quasi-isotropic lay-up. Tape laminate stiffeners were fabricated at Boeing, St. Louis.

Pull-off tests were executed by loading the end of the web at a constant displacement rate while the edges of the skins were simply supported just beyond the ends of the flanges. The span between the load points varied due to the geometric dissimilarity of the two specimen types, but the effects of this difference can be calculated by model analysis. Typical load–displacement curves are shown in Fig. 4. The braided stiffener achieves much higher loads, partly because of the narrower load span, but also, as analysis will show, because of more favourable local stress distributions.

2.1. Failure of tape laminate stiffeners

The first damage event for each specimen was a vertical crack in the noodle (Fig. 1). Next, delamination cracks occurred in first one then the other of the radii (Fig. 1). These cracks grew into the skin and web as

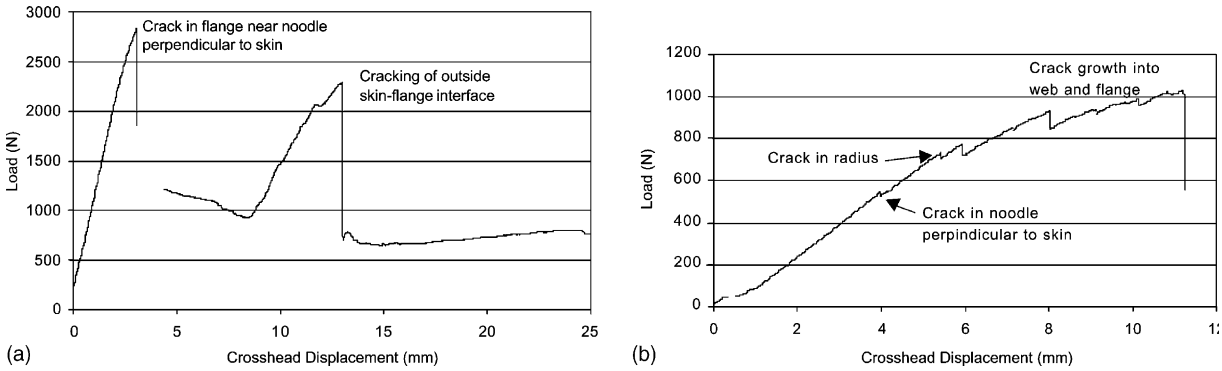

Fig. 4. Load–displacement curves for (a) a braided stiffener; (b) a tape stiffener.

Fig. 5. Post mortem micrograph of a 60k 3D-braided stiffener showing location of first cracking in the flange (1), multiple cracking in the flange (arrows), later crack near skin/flange interface (2), and broken knitted tows adjacent to the skin–flange interface (encircled).

the load was increased. Cracks initiating at the outside skin/flange interface were also noted later in the experiments. These latter cracks did not grow substantially prior to specimen failure.

The effect of z-pins on the failure sequence for the tape laminate stiffeners was reported previously (Rugg et al., 2002). In the presence of z-pins and for loading configurations similar to those used here, the initial delamination is always in the radius portion of the T. These cracks grow down into the web of the T. The next stage of damage is delamination within the skin directly above the delaminated radius section. This skin crack is arrested by the z-pins. Multiple delaminations form in the skin, followed by cracking of the noodle material and compressive microbuckling of the plies in the skin (consistent with kink band failures). The sequence of steps to failure is typified by Fig. 2.

2.2. Failure of 3D-braided stiffeners

The failure sequence was observed in two 3D-braided specimens, one braided with coarse, 60k denier tows, the other with finer, 12k denier tows. The first damage event for the 60k-tow specimen was a vertical crack in the flange near the web (Fig. 5). A large load drop in the load–displacement curve accompanied this event (Fig. 4a). The crack propagated along multiple paths, often, but not always, along tow boundaries. The crack did not penetrate into the skin and appeared to arrest at the skin–flange boundary. Effects of the 3D reinforcement characteristics of the braid are evident as loading continued: fiber tows were observed bridging the initial crack and the machined, side surfaces of the specimen were distorted by the action of tows that intersected them obliquely. Eventually the load increased steeply again until a crack initiated at the outside skin–flange interface. This crack is not precisely at the interface between the braided flange and the skin, but above the first ply of the skin: broken tows that were used to knit the skin are visible on the fracture surfaces (Fig. 5).

No cracking was observed in the 12k-braided stiffener. Failure in those specimens occurred by localized buckling of the skin. Finer denier textiles are generally expected to be less vulnerable to microcracking, but the result that the fine denier stiffener outlasted the skin in the pull-off test is quite remarkable.

3. Strain distributions

3.1. Experiments

Full-field displacements on the end sections of specimens were monitored with speckle interferometry. Speckle arises in a reflected laser beam because of optical roughness on the reflecting surface. In the setup used, a helium–neon laser beam is divided into two illumination beams that illuminate the object from

equal and opposite angles. A CCD camera records the superposition of the two reflected fields. The mirror in one of the illumination beams is piezoelectrically actuated to step the phase of that beam by 90° between successive scans (image frames). Analysis of the phase-stepped images yields saw-toothed, gray scale fringes that give the magnitude and direction of the differential displacement caused on the specimen surface by a change in applied stress. The configuration described is sensitive only to the in-plane displacement of the object at right angles to the bisector of the two illumination beams. Thus separate experiments have to be performed to obtain displacement data parallel and perpendicular to the web of the stiffeners. In order to avoid decorrelation of fringes (due to over-large specimen translation), displacement fringe patterns were obtained at appropriately small load intervals. Increments of displacement were added together to get the displacements over wider load ranges. Strain was calculated by numerical differentiation. The sensitivity of the displacement measurements was about 100 nm, one-tenth of the fringe spacing. The image size was typically of the order 50×50 mm, giving a pixel size (spatial resolution) of approximately 100 μm (with 512×480 pixels).

3.2. Model formulations

A conventional finite element model was formulated to analyze the 2D tape laminate T-stiffener, while the Binary Model was used to analyze the 3D-braided T-stiffener. Details are as follows.

3.2.1. Tape laminate stiffener

For the tape laminate T-stiffener, traditional finite element methods with standard continuum elements were used for both the web and the flanges. The mesh is illustrated in Fig. 6. Only half of the T-stiffener was modeled owing to its symmetry. Since the web, flanges, and skin were fabricated as quasi-isotropic lay-ups, they were assigned transversely isotropic material properties, with the pole direction normal to the laminate plane. In the radii, a cylindrical coordinate system was used to assure that the pole direction remains normal to the local laminate plane. The noodle region was modeled as isotropic resin material. The material properties of the laminates and the resin are listed in Table 1.

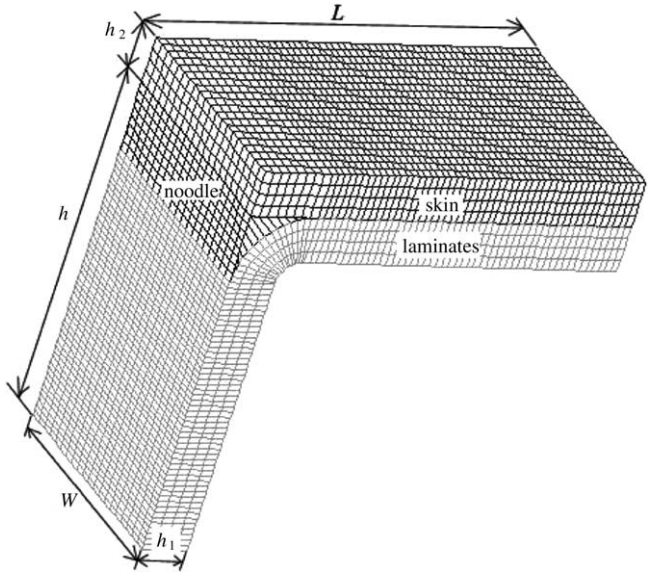

Fig. 6. FEM model for the 2D tape laminate T-stiffener, only half of the stiffener was modeled due to its symmetry.

Table 1
Properties of constituent materials in the 2D tape laminate T-stiffener

Skin and laminate components				
In-plane modulus (GPa)	In-plane Poisson's ratio	Out-of-plane shear modulus (GPa)	Out-of-plane Young's modulus (GPa)	Out-of-plane Poisson's ratio
60	0.1	4.0	10.0	0.3
Resin				
Young's modulus (GPa)	Poisson's ratio			
3.0	0.3			

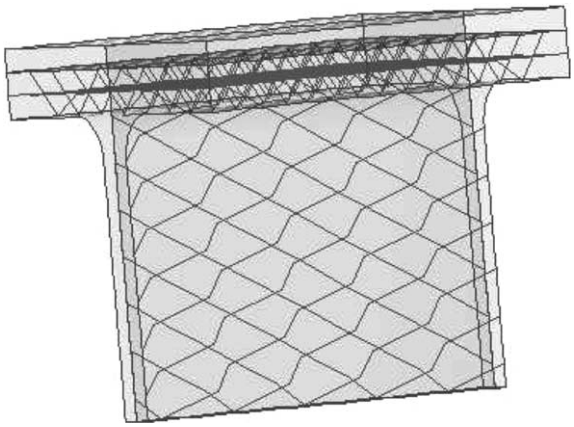

Fig. 7. Binary model of the 3D-braided T-stiffener: the lines represent the geometric center of fiber tows; the solid represents the effective medium which was discretized into 8-node 3D brick elements (not shown in the figure).

The geometric dimensions of the tape laminate stiffener, in the notation defined in Fig. 6, are: $L = 50$ mm; $W = 27$ mm; $h = 50$ mm; $h_1 = 2$ mm; $h_2 = 4$ mm; $r = 5$ mm.

3.2.2. Binary model of 3D-braided T-stiffener

The 3D-braided T-stiffener was analyzed by the Binary Model. Two meshes are required for the Binary Model, viz., 1D "tow" elements representing the axial stiffness of fiber tows in the 3D architecture; and 3D "effective medium" elements representing matrix-dominated properties (Fig. 7). The two meshes were generated independently and then integrated in ABAQUS (V6.2) [3] using the "embedded element" function. The entire braided T-stiffener has to be modeled because it does not have the same symmetry as the 2D tape laminate T-stiffener: the fiber tow arrangement near the web/flange junction is not symmetrical about the mid-plane (Fig. 3a). The skin material was the same as for the tape laminate stiffener.

The elastic material properties of constituent fibers and matrix for the 3D-braided stiffener are listed in Table 2. From these properties and the fiber volume fraction, the elastic properties for the 1D tow elements and the 3D effective medium elements can be calculated. Details of the generic formulation of the Binary Model may be found in Xu et al. (1995) and Cox and McMeeking (2002). The particular model parameters for the 3D-braided stiffener are defined in Appendix A.

[3] Hibbitt, Karlsson, and Sorensen, Inc., Pawtucket, RI 02860.

Table 2
Properties of the constituent materials in the 3D-braided T-stiffener

Composite/binary model		Volume fraction (%)	Apparent fiber angle (deg)	Young's modulus (GPa)	Poisson's ratio
Composite	Fiber[a]	70	30	230	0.3
	Matrix[b]	30	–	3.0	0.3
Binary model	1D tow elements	–	–	214[c]	–
	Effective medium elements	–	–	16	0.3

[a] Thornel® Carbon Fiber T-300, Amoco Performance Products, Inc. Atlanta, GA.
[b] Epo-thin, Buehler Co., Deuschland, UK.
[c] The Binary Model is formulated with tow elements represented by a spring constant, k_t, which is related to the Young's modulus quoted here by $k_t = EA$, with A the tow's cross-sectional area. In fact, A and E do not appear independently in the calculation, even though ABAQUS requires their input. A is defined to ensure the correct total fiber count in the tow.

3.3. Experiment vs. theory

Comparisons are presented here of the predicted and measured strains before the onset of cracking in the tape laminate and 3D-braided T-stiffener/skin specimens. The case shown for the 3D-braided stiffener is the one braided with 60k denier tows. Predictions and measurements for the stiffener braided with 12k denier tows were very similar. (Differences in the behaviour of the fine and coarse denier stiffeners were pronounced only beyond the proportional limit.) Numerical simulations were executed using properties for representative carbon fibers in an epoxy matrix. Output from the simulations was plotted first as the maximum principal strain and then as the two particular strain components that were measured by speckle interferometry. These two strain components were the strain component in the flange direction, ε_1, and the strain component along the web direction, ε_2.

The maximum principal strain is plotted as absolute strain values for a load equal to the measured failure load in each case (see Section 4 for further analysis). The individual strain components, on the other hand, are plotted in normalized form: ε_1 has been normalized by the maximum compressive strain (absolute value) in the topmost layer of the skin; while ε_2 has been normalized by the average tensile strain in the web far from the junction.

3.3.1. Tape laminate stiffener

Fig. 8 shows the predicted distribution of the maximum principal strain in the tape laminate stiffener and skin. The strain is maximum in the noodle, which is relatively compliant, and in the radius adjacent to the noodle. The strain in the cusp of the noodle exceeds the far-field strain in the web by a factor of approximately 14. The location of the maximum principal strain coincides with the trajectory of the crack seen in the noodle (Fig. 1b). Failure initiation in the noodle is not well understood, but some recent studies indicate that, in such a resin pocket, initiation correlates reasonably well with a critical value of stress or strain existing over a certain gauge length (Clarke and McGregor, 1993; Sheppard et al., 1998; Feih et al., 2001). The gauge length depends on the ductility of the material.

The strain in the radius of the stiffener is approximately 4–5 times the far field strain in the web. Once again, the location of the concentration coincides with observed cracking (radius crack in Fig. 1b).

Fig. 9 compares the normalized measured and predicted strain components, ε_1 and ε_2, for the tape laminate T-stiffener. [4] Since the extreme values of predicted strains take values beyond the range of the

[4] The model dimensions used in preparing Figs. 9 and 11 were slightly different to those of the tested specimens, but this had no effect on the calculated *normalized* strains in the noodle or junction regions.

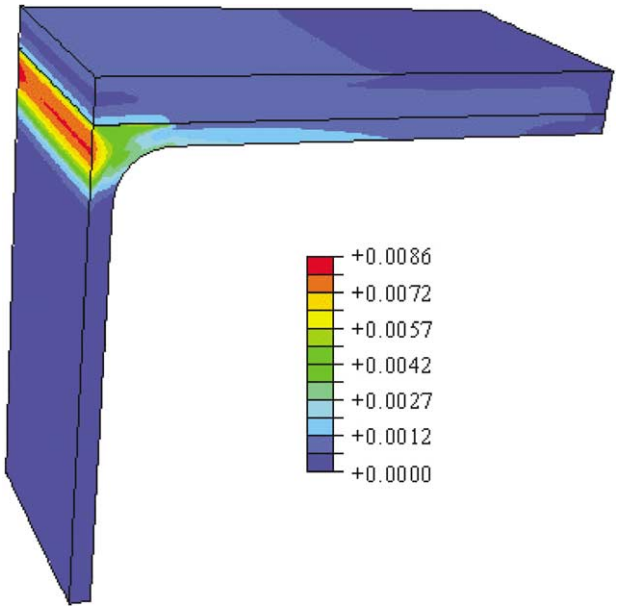

Fig. 8. Predicted maximum principal strain distribution in the 2D tape laminate T-stiffener at the measured failure load.

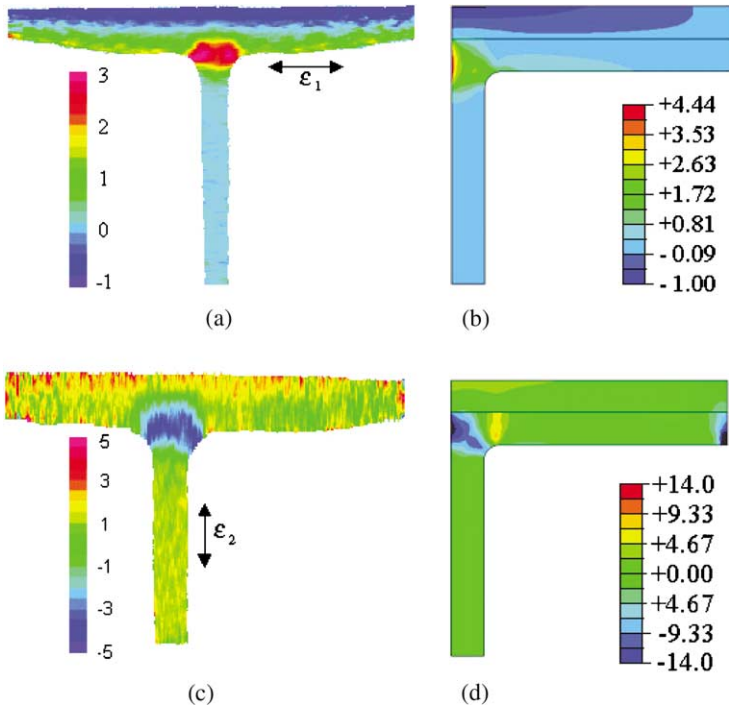

Fig. 9. Comparison of experimentally obtained (a, c) and numerically predicted (b, d) strains for the 2D tape laminate stiffener. (a, b) show strain component ε_1, (c, d) show strain component ε_2.

experimental measurements, different color codes for strain values have been used in this figure for the experiments and predictions. The extreme strain values appearing in the predictions are confined to small volumes, which would have been beneath the resolution of the measurements. Agreement otherwise between measurement and theory is very good. In particular, the model predicts the large strain concentrations in the noodle region quite well. A region in which ε_1 is high covers almost all the noodle region, with an average normalized strain value of about 3.0 (Fig. 9b). This is in excellent agreement with the experimental measurement (Fig. 9a). The noodle region is also subject to a concentrated compressive strain in the web direction, $\varepsilon_2 < 0$ (Fig. 9d). This again corresponds well to the experimental result (Fig. 9c), both qualitatively and quantitatively.

The large strain concentrations in the noodle region are caused by the modulus mismatch between the laminate composite and the epoxy resin. During a pull-off test, the laminate in the radius tends to straighten and move along the positive x-direction. The epoxy in the noodle region has little constraining effect against this motion because of its low modulus and develops large strain (large ε_1). The epoxy is also compressed in the web direction, because the skin immediately above the noodle region bends and moves downward.

The high strain concentration region is not limited to the noodle. It also includes most of the laminate composite in the radius, which has low transverse modulus.

3.3.2. 3D-braided stiffener

Fig. 10 shows the maximum principal strain distribution in the 3D-braided T-stiffener predicted by the Binary Model. The strain in the web is fairly uniform. There are strain concentrations in the web-flange junction region, but the maximum strain concentration factor (relative to the far-field strain in the web) is only $\approx$6, at a location on the flange just outside the junction region. Most of the junction region shows a significantly smaller strain concentration. The moderate magnitude and spatial extent of strain concentrations in the 3D-braided T-stiffener form a strong contrast to the tape laminate stiffener. The effective avoidance of strain concentration is a consequence of the 3D architecture: in this particular design and for the pull-off loading configuration, the stiffener is uniformly compliant. The fiber tows throughout the stiffener tend to lie along directions that are not closely aligned with load paths. [5] The tape laminate stiffener, on the other hand, exhibits strong elastic heterogeneity: the material is locally stiff in the fiber direction in the web and radii, where significant stresses arise; but locally compliant in the noodle and in the radii transverse to the fiber direction, where significant stresses also arise. The resultant strain nonuniformity leads to high strain concentration factors.

Fig. 11 shows the normalized measured and predicted values of ε_1 and ε_2 for the 3D-braided T-stiffener. Because the experimental and predicted strains cover similar ranges for either ε_1 or ε_2, a single color code has been used for each strain component in this figure. The experimentally measured strains show that the only strain concentration that arises in the junction region is a moderate tensile strain (normalized strain value $\approx$ 2.0) at the corner for the strain component ε_1 (Fig. 11a). For strain in the web direction, ε_2, there is no obvious strain concentration throughout the whole specimen (Fig. 11c).

Fig. 11b and d shows values of ε_1 and ε_2 predicted by the Binary Model for the 3D-braided T-stiffener, which are in excellent agreement with experiment. For example, the predicted maximum normalized strain, ε_1, occurs at the flange near the radius, which is the exact location observed in the experiment. Moreover, the predicted normalized strain value of 2.0 matches quantitatively with the experimental value. The

[5] While in this particular loading configuration strong spatial fluctuations in strain are not present, they are pronounced in other cases. For example, the Binary Model reveals strong fluctuations, correlated with the local tow architecture, in thermal residual strains in the same 3D-braided stiffeners. The prediction of relative featurelessness in the pull-off strain fields by a model that has the capacity for determining local spatial fluctuations is a successful validation test.

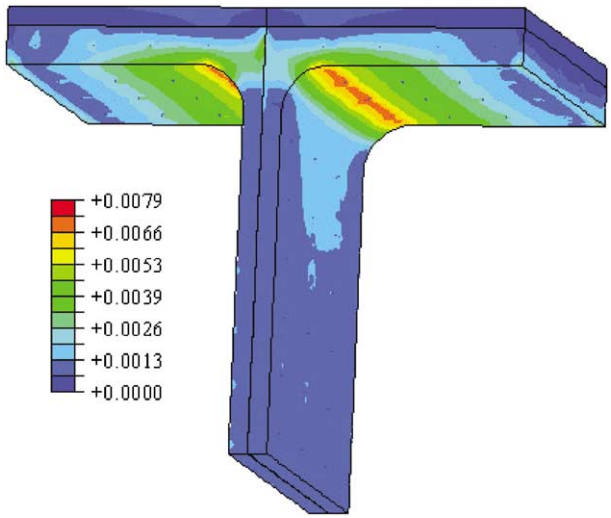

Fig. 10. Predicted maximum principal strain distribution in the 3D-braided T-stiffener at the measured failure load.

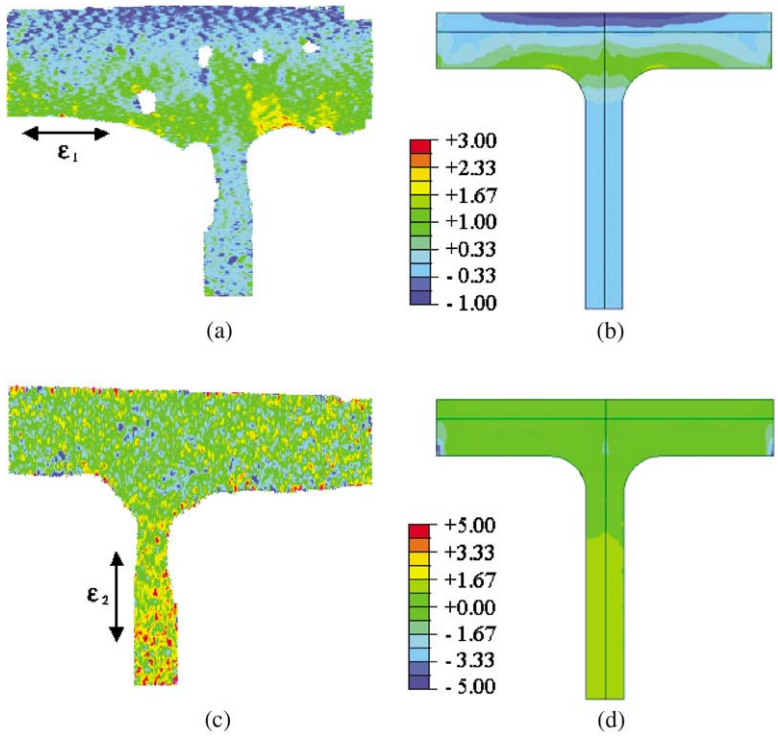

Fig. 11. Comparison of experimentally obtained (a, c) and numerically predicted (b, d) strains for the 3D-braided T-stiffener. (a, b) show strain component ε_1, (c, d) show strain component ε_2.

predicted ε_2 (Fig. 11d) also agrees well with the experimental result (Fig. 11c) (ignoring the high strain dots, which are measurement noise, beneath the spatial resolution of the method).

4. Analysis of first failure and design implications

A remarkable observation is that the pull-off failure load is much higher for the 60k 3D-braided stiffener than for the tape laminate stiffener (2800 N vs. 510 N—see Fig. 4). Here some additional model analyses are used to explore the implications of these data.

The question of which combination of local strain or stress components should be used to establish a criterion for matrix-mediated local failure events in composites, especially with 3D textile reinforcement, remains open. Provided the material is not too brittle, the strength-determining matrix fracture process will generally involve the development of a process zone, e.g., a craze zone in the polymer matrix, which is typically ~1 mm long. Deformation within the craze zone often occurs at an approximately constant and uniform stress state, which implies uniform strain in adjacent elastic material. Provided original flaws (e.g., sharp voids or cracks) are not much larger than the process zone, the critical condition for cracking may be approximated by attainment of this stress or strain over an appropriate gauge length. This is because initiation of the process zone tends to be a stable process, during which the stress in the zone is not far from invariant (an idea originating with Dugdale's work on metal, but also a fair approximation for craze zones). Unstable crack propagation begins only when material at the trailing end of the zone begins to fail. Consistent with this depiction, engineering analyses of crack initiation in polymer composite joints have suggested the best correlation with test data is found with a gauge length that is also of order ~1 mm (Clarke and McGregor, 1993; Sheppard et al., 1998; Feih et al., 2001).

The distributions of two strain measures were examined, namely the maximum principal strain, ε_{max}, and the first strain invariant, $J_1 \equiv \varepsilon_{11} + \varepsilon_{22} + \varepsilon_{33}$. Simulations were executed using the dimensions of the tested specimens, as specified in Section 3 and Appendix A, and the measured loads to the first failure event. The predicted spatial distributions of ε_{max} at the failure load are shown in Figs. 8 and 10. The distributions of J_1 were similar to those for ε_{max} in both stiffeners and the locations of the maximum values of J_1 also coincided with the observed first failure sites. The computed absolute values of ε_{max} and J_1 at the sites of peak strain concentration were as shown in Table 3.

The maximum strain at the failure load averaged over a gauge length of 1 mm along the cracking direction was also calculated for both stiffeners (Table 3). Following the arguments laid out above, the spatially averaged strain measure might be regarded as a critical value for failure. Since the values in Table 3 are calculated at the failure load, they may be regarded as representing experimentally deduced critical values for the observed failure mechanisms, namely tensile noodle cracking (tape laminate stiffener) and matrix cracking between tows (braided stiffener). The fact that higher values are found for this critical quantity in the tape laminate stiffener could imply that the resin is superior in that laminate. In fact, the resin used to consolidate the 3D-braided stiffener is not believed to be particularly strong.

Table 3
Computed values of strains at failure sites at first failure load

	3D-braided stiffener (%)	Tape laminate stiffener (%)
Maximum principal strain, ε_{max}	0.79	0.87
First strain invariant, J_1	0.34	0.50
ε_{max} averaged over 1 mm gauge	0.60	0.87

The inferred critical averaged strain is similar to the critical point strain for the tape laminate stiffener, but significantly less in the 3D-braided stiffener. Averaging has a greater effect in the latter, because of the greater degree of localization of the strain concentration.

The inferred critical strain for the tape laminate specimen was used to investigate the effect of specimen size on the critical pull-off load. Because of the different manufacturing sources of the two types of stiffener, the supporting span of the tape laminate stiffener ($2 \times 50 = 100$ mm) is about twice that of the braided stiffener (54 mm). A second simulation was therefore executed for the tape laminate stiffener, using a reduced span of 54 mm. The pull-off load required to achieve $\varepsilon_{max} = 0.87\%$ in the center of the noodle rose to 1100 N, but this is still a factor of 2.6 below the load to first failure of the braided stiffener (2800 N).

The residual difference in pull-off loads (1100 vs. 2800 N) can come from two sources. One is the difference in resin type used to fabricate the two stiffeners, the other is the difference in fiber architecture. The role of the resin is difficult to quantify precisely, because independent toughness data for either the resins themselves or composites containing them are unavailable. Nevertheless, some plausible deductions are possible. The inferred critical strains of Table 3 imply that the difference in the resins is not all that great; some error in the method used to deduce the critical values that would disguise a much greater disparity seems unlikely. To assess the effects of fiber architecture, the strain concentration factors for the two stiffeners were calculated from the output of the simulations. The peak strain concentration factors based on spatially averaged strains (maximum value relative to the far-field in the web) were 5 in the 3D-braided stiffener and 14 in the tape laminate stiffener. Thus the ratio of concentration factors based on spatially averaged strains was approximately 2.8. This is of the same order as the measured difference in the pull-off loads and strongly suggests that the reinforcement architecture has played the major role in strengthening the component.

5. Conclusions

In the 3D-braided stiffener chosen for study, the mechanisms of premature cracking that plague traditional 2D tape laminate T-stiffeners were avoided. Furthermore, a large strength improvement of the braided stiffener with regard to junction failure in pull-off tests was measured relative to a tape laminate stiffener. The advantage of the 3D-braided stiffener in pull-off seems to be that strain concentrations are minimized by the favourable tow deployment. The 3D-braided stiffener contains no analogue of the deleterious noodle region and radius segments in a tape laminate stiffener.

The particular architecture of the subject 3D-braided stiffener contained no straight axial tows (aligned along the length of the stiffener). Therefore, tests of axial or bending stiffness or strength would show the braided stiffener inferior to the tape laminate stiffener. However, in the 3D braiding apparatus described by Bogdanovich and Mungalov (2002), for example, the incorporation of axial tows is straightforward. Similar axial and bending properties to those of tape laminate stiffeners could be achieved. Furthermore, the presence of axial tows, which are transverse to pull-off loads, would be expected to have only a minor effect on the favourable distribution of strains demonstrated here during pull-off loading. Axial tows should therefore not degrade the robustness of the braided stiffeners under pull-off.

The ability of the Binary Model to deal with the effects of a complex 3D reinforcement architecture has been demonstrated by validated strain analysis of the 3D-braided component. The modest strain concentrations predicted in the junction region were confirmed by full field strain measurements. Since the Binary Model allows direct correlation of local strain variations with the textile architecture, its use as an optimization tool for virtual design studies is supported. The high cost of the conventional cycle of designing, fabricating, and testing textile composites can be greatly reduced. Because of the capacity of the Binary Model for simulating significant volumes of a component, virtual design can be carried out at the structural rather than the material level.

Acknowledgements

The authors are very grateful to the Boeing Company for supporting this work under a rolling contract with Rockwell Scientific. Mr. John Townsley of the Boeing Company provided very helpful guidance in formulating the problem and arranged fabrication of the tape laminate stiffeners. Drs. Alex Bogdanovich and Dmitri Mungalov of 3TEX Inc. very graciously supplied the 3D-braided stiffener preforms and computer drawings with detailed information on fiber architecture.

Appendix A. Binary model setup for the 3D-braided T-stiffener

A FORTRAN program was coded to generate the 1D line elements and the associated node coordinates for the 3D-braided T-stiffeners shown in Figs. 3a and 12. The following parameters, defined in Fig. 12, are input interactively:

1. the total width of the flange, W;
2. the braid angle, α;
3. the thickness of the flange (assumed the same thickness for the web), *TTH*;
4. the number of tows crossing any section of the flange, *NTOW_Y*. There are, for example, two tows at each filled dot in Fig. 12(a) and one tow at each open dot.
5. the number of tows crossing any section of the web, *NTOW_Z*. There are, for example, two tows at each filled dot in Fig. 12(b) and one tow at each open dot.
6. the number of cross-sections that need to be modeled, *NT_MX*.

With these parameters being input, the program will calculate the model length, L, and the height, H, automatically. A file is generated that contains all the nodal numbers and coordinates and the 1D line element connectivity. This file can then be integrated into an ABAQUS input file that defines the effective medium and skin (3D solid elements). The 1D-element set can then be embedded into the solid element set

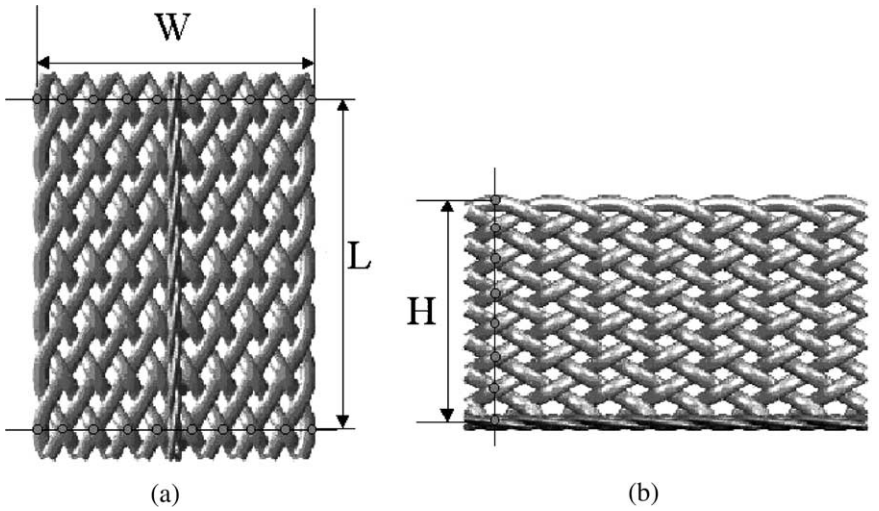

Fig. 12. Computer model of the 3D-braided T-stiffener preform (courtesy D. Mungalov, 3TEX, Inc.), with nomenclature added for present paper. Views of (a) flanges and (b) web.

using the "* EMBEDDED ELEMENT" function. In simulations of the strain distribution at failure of the 60k denier braided stiffener, the parameter values were:

$W = 54.0$ mm;
$\alpha = 30°$;
$TTH = 4.0$ mm;
$NTOW\_Y = 18$;
$NTOW\_Z = 14$;
$NT\_MX = 7$,

which lead to $L = 34.64$ mm and $H = 42.0$ mm.

In addition, the skin has the same in-plane dimensions as the flange (36.64 mm × 54.0 mm) but a thickness of 2.0 mm.

References

Bogdanovich, A.E., 1993. Three-dimensional analysis of anisotropic spatially reinforced structures. Composites Manufacturing 4, 173–186.

Bogdanovich, A.E., Mungalov, D., 2002. Innovative 3-D braiding process and automated machine for its industrial realization. In: Proceedings of the 23rd International SAMPE Conference, Paris, April 2002, pp. 529–540.

Clarke, J.D., McGregor, I.J., 1993. J. Adhesion 42, 227–245.

Cox, B.N., Carter, W.C., Fleck, N.A., 1994. A binary model of textile composites. I. Formulation. Acta Metall. Mater. 42 (10), 3463–3479.

Cox, B.N., McMeeking, R., 2002. The Binary Model—User's Guide. Edition 2.1. Rockwell Scientific, Thousand Oaks, California, USA.

Feih, S., Shercliffe, H.R., McGrath, G., 2001. Quality assessment and design guidelines for adhesively bonded peel-joint geometries in composite aerospace structures. In: Proceedings of the Sixth International Conference on Deformation and Fracture of Composites, Manchester, UK, April, 2001. IOM Communications, London.

Freitas, G., Magee, C., Dardzinski, P., Fusco, T., 1994. Fiber insertion process for improved damage tolerance in aircraft laminates. J. Adv. Matls. 25 (4), 36–43.

Freitas, G., Fusco, T., Campbell, T., Harris, J., Rosenberg, S., 1996. Z-fiber technology and products for enhancing composite design. In: AGARD conference proceedings, 17-1-8.

Rugg, K.L., Cox, B.N., Massabò, R., 2002. Mixed mode delamination of polymer composite laminates reinforced through the thickness by Z-fibers. Composites A 33 (2), 177–190.

Sheppard, A. et al., 1998. Int. J. Adhesion Adhesives 18, 385–400.

Xu, J., Cox, B.N., McGlockton, M.A., Carter, W.C., 1995. A binary model of textile composites. II. The elastic regime. Acta Metall. Mater. 43 (9), 3511–3524.

Yang, Q.D., Rugg, K.L., Cox, B.N., Marshall, D.B., 2002. Validated Predictions of Macroscopic and Local Strains in a 3D C/SiC Weave, J. Am. Ceram. Soc., submitted.